Heliyon 10 (2024) e26341

Contents lists available at ScienceDirect

Heliyon

journal homepage: www.cell.com/heliyon

Research article

Synthesis, optical properties, DNA, β-cyclodextrin interaction, hydrogen isotope sensor and computational study of new enantiopure isoxazolidine derivative (ISoXD)

Afnan Alotayeq [a], Siwar Ghannay [a], Ibrahim A. Alhagri [a,b], Iqrar Ahmed [c,d], Bechir Hammami [a], Abuzar E. A. E. Albadri [a], Harun Patel [d], Sabri Messaoudi [a,e], Adel Kadri [f,g], Sadeq M. Al-Hazmy [a], Kaiss Aouadi [a,h,*]

[a] *Department of Chemistry, College of Science, Qassim University, Buraidah 51452, Saudi Arabia*
[b] *Department of Chemistry, Faculty of Sciences, Ibb University, Ibb, Yemen*
[c] *Department of Pharmaceutical Chemistry, Prof. Ravindra Nikam College of Pharmacy, Gondur, Dhule, 424002, India*
[d] *Division of Computer Aided Drug Design, Department of Pharmaceutical Chemistry, R. C. Patel Institute of Pharmaceutical Education and Research, Shirpur, 425405, Maharashtra, India*
[e] *Faculty of Sciences of Bizerte, Carthage University, Jarzouna, Bizerte 7021, Tunisia*
[f] *Faculty of Science of Sfax, Department of Chemistry, University of Sfax, B.P. 1171, 3000 Sfax, Tunisia*
[g] *Department of Chemistry, Faculty of Science and Arts of Baljurashi, Al- Baha University, Saudi Arabia*
[h] *Department of Chemistry, Laboratory of Heterocyclic Chemistry Natural Product and Reactivity/CHPNR, Faculty of Science of Monastir, University of Monastir, Avenue of the Environment, Monastir, 5019, Tunisia*

ARTICLE INFO

Keywords:
Docking
MD simulation
Optical properties
DNA
β-cyclodextrin interaction
DFT

ABSTRACT

A novel isoxazolidine derivative (ISoXD) dye was successfully synthesized and comprehensively characterized. In this study, we conducted a thorough examination of its various properties, including optical characteristics, interactions with DNA and β-cyclodextrin (β-CD), molecular docking, molecular dynamic simulation, and density functional theory (DFT) calculations. Our investigation encompassed a systematic analysis of the absorption and emission spectra of ISoXD in diverse solvents. The observed variations in the spectroscopic data were attributed to the specific solvent's capacity to engage in hydrogen bonding interactions. Remarkably, the most pronounced intensities were observed in glycol, which can establish many hydrogen bonds with ISoXD.

Furthermore, our study revealed a significant distinction in the fluorescence behavior of ISoXD when subjected to different solvents, particularly between $CHCl_3$ and $CDCl_3$. Moreover, we explored the fluorescence intensity of the ISoXD complex in the presence of various metals, both in ethanol and water. The ISoXD complex exhibited a substantial increase of fluorescence upon interaction with different metal ions. The utilization of DFT calculations allowed us to propose an intramolecular charge transfer (ICT) mechanism as a plausible explanation for this quenching phenomenon. The interaction of ISoXD with DNA and β-CD was studied using absorption spectra. The binding constant (K) and the standard Gibbs free energy change (ΔG^o) for the interaction between DNA and β-CD with ISoXD were determined. In docking study, ISoXD exhibited significant docking scores (−6.511) and MM-GBSA binding free energies (−66.27 kcal/mol) within the PARP-1 binding cavity. Its binding pattern closely resembles to the co-crystal ligand veliparib,

* Corresponding author. Department of Chemistry, College of Science, Qassim University, Buraidah, 51452, Saudi Arabia.
E-mail address: K.AOUADI@qu.edu.sa (K. Aouadi).

https://doi.org/10.1016/j.heliyon.2024.e26341
Received 23 November 2023; Received in revised form 12 February 2024; Accepted 12 February 2024
Available online 13 February 2024

and during a 100ns MD simulation, ISoXD displayed strong stability and formed robust hydrogen bonds with key amino acids. These findings suggest ISoXD's potential as a PARP-1 inhibitor for further investigation in therapeutic development.

1. Introduction

Isoxazolidines present a crucial structural motif in many bioactive molecules [1–4], pharmaceuticals [5,6], agrochemicals [7–9], and synthetic intermediates due to N–O bond fragility [10,11]. In our previous work, we have focus on the 1,3-Dipolar cycloaddition (1,3-DC) reaction involving a chiral nitrone derived from (−)-menthone and heterosubstituted (oxygen, nitrogen) alkenes. This nitrone has been engaged in stereocontrolled of 1,3-DC reactions to access enantiopure ISoXD with diversified biological activities, such as antimicrobial [12], antioxidant [13], antidiabetic [14,15] anticancer [16] activities. Also, we have exploited the fragility of the N–O bond of the synthesized isoxazolidines to access unnatural [17] and natural amino acids [18].

Numerous multidisciplinary researches have been conducted on fluorescent compounds such as anthracene, rhodamine, coumarins, and "boron-dipyrromethene" (BODIPY) compounds [19], in addition to ISoXD. Researchers have looked into the compounds' physical characteristics and enhanced their performance as fluorescent compounds in various media. They have also explored the potential applications of these compounds in the fields of electronics, medicine, and the environment, such as chemosensors for trace amounts of heavy metals like Cu, Ni, and Hg (II) [20], and biosensors for gamma radiation [21].

Despite the prevalence of isoxazolidine in the field of imaging probes, they also have attracted much attention recently [22]. However, isoxazolidine was considered as a chemosensor for mercury ions, where the emission maximum fluorescence intensity is quenched of by adding 0–4.0 μL of Hg(II) (1:1 M ratio). ISoXD: Hg (II) in the same time a growth of a new emission peak at 399 nm is observe (blue shift = 82 nm). Also, an ISoXD was used as a photochemical sensor for pH determination. It was observed that the emission intensity increased significantly for the deprotonated form compared to the protonated form [23].

It is important to investigate how small molecules interact with DNA using spectra because it can shed light on the ways in which they influence biological functions. The structure, conformation, and stability of the DNA molecule can be determined using spectroscopic methods, as well as the affinity and specificity of the small molecule's binding to DNA [24]. All this can be used to create novel drugs or improve ones that already exist for higher efficacy and lower toxicity. Additionally, it can help with the comprehension of basic cellular functions like DNA replication, transcription, and repair [25,26].

β-CD is a cyclic oligosaccharide composed of seven glucose units linked by alpha-1,4 glycosidic bonds [27]. It is synthesized by the enzymatic degradation of starch through bacterial enzymes, and its internal cavity structure allows it to form inclusion complexes with a wide range of guest molecules [28]. β-CD is used extensively in the pharmaceutical industry for drug delivery, as its ability to encapsulate hydrophobic compounds enhances their solubility and stability [29–31].

In this work, we wish to obtain new chemical and biological sensors. We also produced a new tunable dye by changing the media dissolved in it to produce radiation at different visible wavelengths with a high fluorescence quantum yield. We present the independent properties of our compound, including optical properties, interactions with DNA and β-CD, hydrogen isotope characteristics, and computational study.

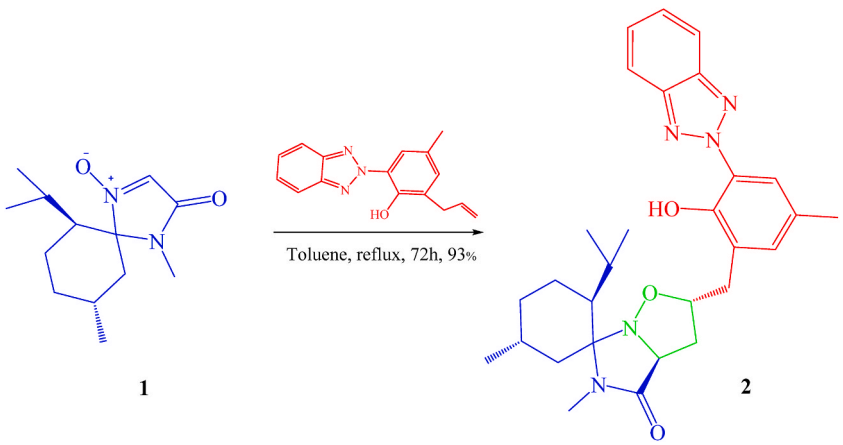

Scheme 1. Synthesis of ISoXD **2**.

2. Results and discussion

2.1. Chemistry

Chiral nitrone **1** reacts with 2-allyl-6-benzotriazol-2-yl-4-methyl-phenol, commercial from Aldrich, *via* 1,3-DC to give isoxazolidine **2** with a yield of 93% (Scheme 1).

The isoxazolidine ring was formed with the simultaneous creation of two asymmetric centers C_3* and C_5*. The structural identification of the ISoXD **2** was carried out by exploiting the results of the 1D and 2D NMR such as 1H, 13C and NOESY 2D. Indeed, the comparison of the coupling constants with the data of the literature between the protons H3–H4proR, H4proS-H5 and H4proS-H5 (Table 1) shows that the protons H3–H4proR and H5–H4proS move in the same direction, whereas the H5–H4proR protons are in trans.

In addition, the 2D NOESY spectrum of compound **2** shows a strong correlation between H3–H4proR and H5–H4proS protons and a weak NOE effect between H5–H4proR. These observations further support the stereochemistry of compound **2** proposed in Fig. 1.

2.2. UV–Vis absorption and fluorescence spectra

The ISoXD exhibits a relatively strong absorbance at 221 nm in ethanol, primarily attributable to the spin-allowed $S_0 \rightarrow S_2$ transition. The lower-intensity bands observed at longer wavelengths, namely 306 nm and 348 nm, are associated with the spin-allowed $S_0 \rightarrow S_1$ transition of the hydroxyphenyl benzotriazole group [32,33]. A noticeable blue shift to 340 nm in the absorbance, corresponding to the $S_0 \rightarrow S_1$ peak, is observed when the solvent is changed to H_2O. This shift is ascribed to the stronger hydrogen-bonding interactions between the lone pair of electrons on the C═O group and water's hydrogen atoms. Water has a pronounced propensity to form multiple hydrogen bonds [34]. The graphical representation of this effect can be seen in Fig. 2. Moreover, this effect becomes more evident in the excited state, leading to a red shift of approximately 10 nm in the emission maximum wavelength when the solvent is H_2O as compared to ethanol.

We also observe an increase in fluorescence intensities, as previously mentioned. This behavior is supported by Fig. 3, in which we do not observe a shift in the absorption maximum wavelength when transitioning from n-heptane to hexane. However, a 4 nm shift occurs when moving from n-heptane to butanol. Notably, the absorption spectra of ISoXD in ethanol exhibit a pronounced blue shift with the addition of a high percentage of water solvent, especially at concentrations of 80–100% H_2O [35]. This shift can be attributed to complex interactions between the molecule and the solvent environment. We can explain this phenomenon by considering the hydrogen bonding capabilities of ethanol and water. Ethanol forms weaker hydrogen bonds when compared to water, and the introduction of water increases the formation of hydrogen bonds between water molecules and ISoXD. The high electrostatic effect of water on the electrons within the molecule can be attributed to its higher polarity in comparison to ethanol, as shown in Fig. 3.

In Fig. 4a and b, fluorescence measurements also reveal a pronounced influence of hydrogen bonding forces. As the percentage of H_2O in the solvent increases, there is a substantial enhancement in the compound's fluorescence intensity, surpassing five times its value in pure ethanol. Furthermore, a noticeable blue shift is observed at the maximum emission wavelength, accompanied by a distinct alteration in the shape of the emission spectrum, as depicted in Fig. 5a and b.

Fig. 5a and b demonstrate a substantial alteration in the geometry of the ISoXD molecule when it is immersed in glycerol, particularly upon photon absorption. This is evident from the loss of vibrational structure within the emission bands [36,37]. In contrast, when we compare this with the electronic absorption band in H_2O, it becomes clear that the change is a result of water's remarkable ability to establish efficient hydrogen bonds with the ISoXD molecule.

The significant Stokes shift observed for the studied compound in different solvents is presented in Fig. 6 and Table 2, likely stemming from the aromatic stabilization of the excited state due to electron delocalization pathways. In Fig. 6, we conclude a direct relationship between the relative polarity of the solvent and the Stokes shift, meaning that the greater the relative polarity of the solvent, the greater the Stokes shift, along with a corresponding increase in the dipole moment upon excitation. This information can serve as an indicator of charge transfer transitions [38,39]. The observed variations in dipole moments can be attributed to the resonance structures of these dipoles. Notably, ISoXD exhibits a larger dipole moment in its excited state (μe) compared to its ground state (μg).

2.3. Hydrogen isotope interaction

Due to the relatively high absorption coefficient of ISoXD, an interesting trend emerged as the concentration in the $CDCl_3$ solvent increased from 1×10^{-4} M (Abs. = 0.47) to 3×10^{-4} M (Abs. = 2.3). The fluorescence intensity of ISoXD decreased by a factor of six

Table 1
Proton coupling constants H3, H4 and H5.

This work	Literature [8,10]
$J_{3\text{-}4proR} = 0$	$J_{3\text{-}4proR} \sim 0$
$J_{3\text{-}4proS} = 8.8$ Hz	$J_{3,4proS} > 6.6$ Hz
$J_{5\text{-}4proR} = 4.4$ Hz	$J_{5,4proR} < 6$ Hz
$J_{5\text{-}4proS} = 9.2$ Hz	$J_{5,4proS} > 8$ Hz

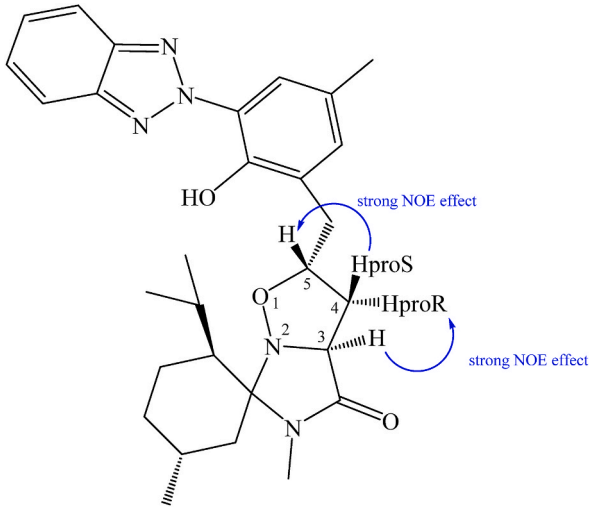

Fig. 1. NOE effect of compound **2**.

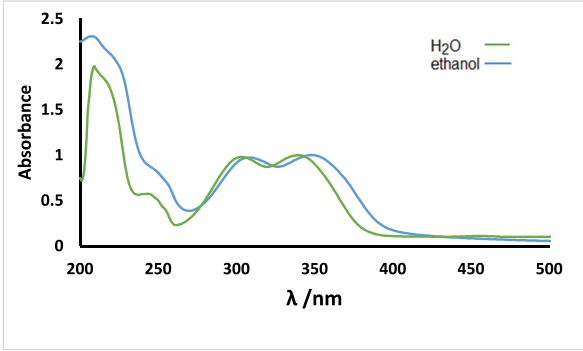

Fig. 2. Absorption spectra of $S_o - S_1$ transition of 1.04×10^{-4} M of ISoXD in EtOH and H_2O.

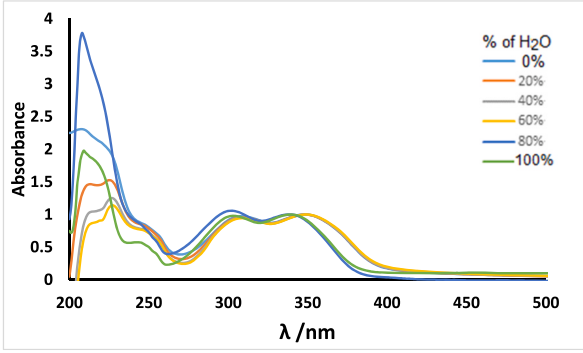

Fig. 3. Absorption spectra of 1.04×10^{-4} M of ISoXD in ethanol at different percentages of H_2O.

compared to that at the lowest concentration, as depicted in Fig. 7. This decrease suggests the occurrence of a quenching phenomenon, likely attributed to the re-absorption of excitation photons, known as the inner filter effect, when the concentration exceeds 1×10^{-4} M [40]. This observation underscores that utilizing higher concentrations of ISoXD is not advantageous. A similar effect was also noted when $CHCl_3$ was used as the solvent. Additionally, a noteworthy increase in emission intensity was observed when transitioning from $CHCl_3$ to $CDCl_3$, owing to the heavy atom effect associated with deuterium compared to hydrogen. A slight blue shift of approximately 4 nm is evident in both emission and absorption spectra, possibly arising from orbital electron redistribution (see Fig. 8 and Table 2). This shift allows for the differentiation of the chloroform solvent from its $CDCl_3$ counterpart.

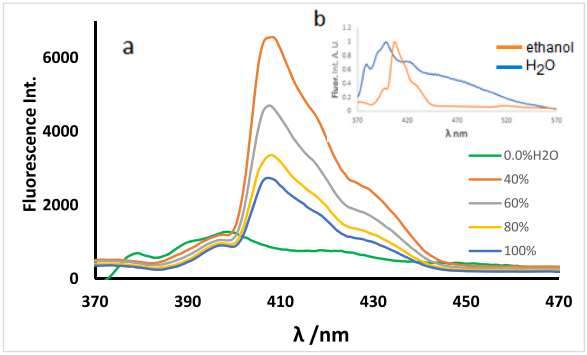

Fig. 4. **a:** Fluorescence spectra of 1.0×10^{-4} M of ISoXD in ethanol, increasing in fluorescence intensities at increasing % of H_2O. and **b:** Normalized fluorescence spectra of ISoXD in ethanol and H_2O.

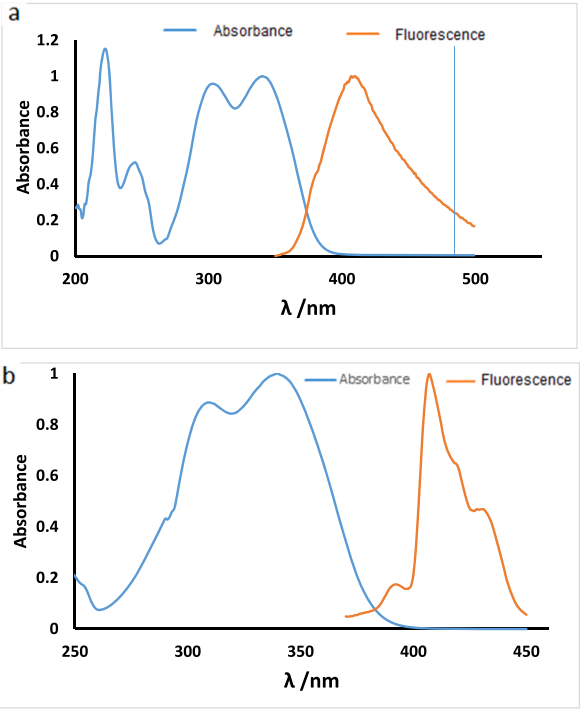

Fig. 5. Normalized absorption and fluorescence spectra of 1×10^{-4} M in a: glycerol, and b: in H_2O, $\lambda_{ex} = 340$ nm.

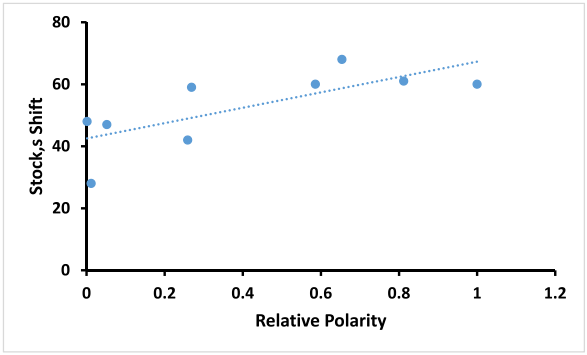

Fig. 6. Effect of relative polarities of the solvents on Stock's shift of 1×10^{-4} M of ISoXD.

Table 2
Measured maximum absorption (λ_{abs}), emission wavelengths (λ_{em}), photochemical quantum yield (ϕ_c), fluorescence quantum yield (ϕ_f) and stck's shift values for ISoXD in different solvents.

Solvents	$\lambda_{abs,\ max}$ (nm)	$\lambda_{em,\ max}$ (nm)	ε	Δf	ϕ_c	ϕ_f	Stock's Shift
n-heptane	345	382	1532	0.012		0.008	28
CCl_4	346	393	17180	0.052	0.05	0.08	47
hexane	345	393	1532	0.0014		0.01	48
$CHCl_3$	344	406	16590	0.259	0.07	0.11 42	
CH_2Cl_2	342	401	18272	0.269	0.06	0.03 59	
CH_3CN	339			0.460			
EtOH	348	409	16318	0.654	0.03	0.02 68	
CH_3OH	339	409	13627	9436		71	
Glycerol	341	407	13045	0.812	0.06	0.22 65	
Butanol	341	409	15309	0.586		0.20 60	
H_2O	340	400	16545	1	0.07	0.1 60	

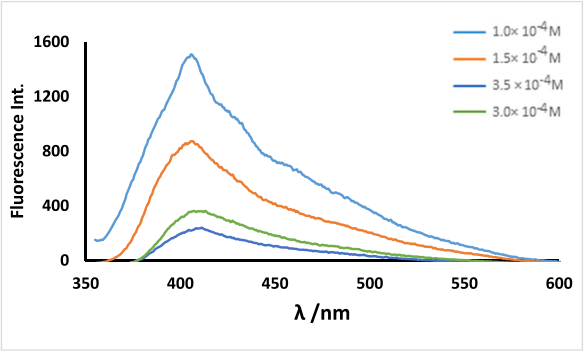

Fig. 7. Fluorescence spectra of 1×10^{-4} M ISoXD in $CDCl_3$ decreasing fluorescence intensities at increasing dye concentrations, $\lambda_{ex} = 340$ nm.

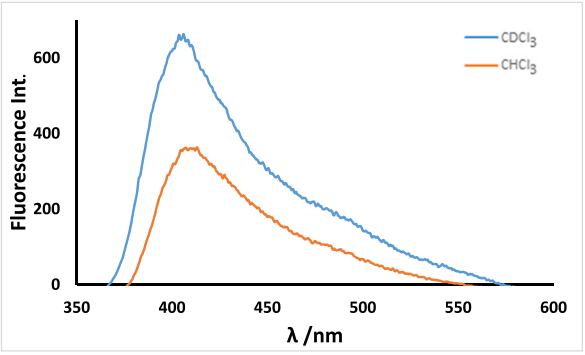

Fig. 8. Fluorescence spectra of 3.12×10^{-4} M of ISoXD in $CDCl_3$ and $CHCl_3$ solvents $\lambda_{ex} = 340$.

2.4. Effect of medium viscosity and hydrogen bonding

The low fluorescence quantum yield (0.02) of ISoXD in ethanol solvent is attributed to its high flexibility, which results in non-radiative energy loss processes. The emission intensity increases by a factor of ten at the maximum emission wavelength due to the rise in the medium's viscosity when transitioning from 0 to 100% glycerol concentration, as illustrated in Fig. 9 and Table 3. Consequently, the fluorescence quantum yield becomes 0.22, primarily due to the imposition of molecular rigidity in the viscous medium, leading to a reduction in non-radiative processes, specifically internal conversion (IC) and vibrational cascade (VC). The presence of additional hydroxyl groups in glycol enables the formation of hydrogen bonds with the O–H and neighboring N–O moieties within the molecule. Additionally, it restricts dihedral rotations in the flexible regions of the molecule. These effects collectively result in a significant enhancement in emission efficiency in glycerol compared to the scenario where water content is increased. This leads to an increased fluorescent quantum yield of the studied dye.

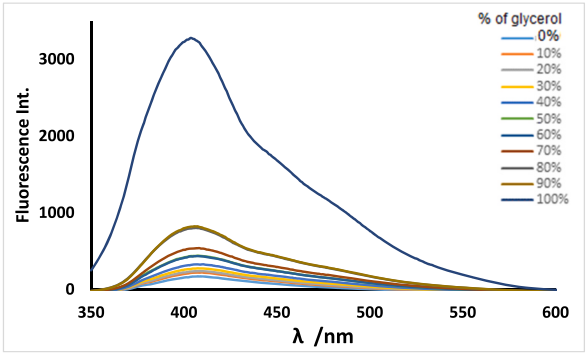

Fig. 9. Fluorescence spectra of 1×10^{-4} M ISoXD in different percentages of glycerol in ethanol, increasing in fluorescence intensities at increasing glycerol, $\lambda_{ex} = 340$ nm.

Table 3
Fluorescence intensities of ISoXD in different % of Glycerol in EtOH.

% of Glycerol	0	10	20	30	40	50	60	70	80	90	100
Fluor. Intesity.	170.15	220.58	238.81	274.09	327.76	440.77	435.15	538.71	802.23	822.91	3276.90

2.5. Interaction with metal ions

In ethanol, upon the addition of equivalent concentrations of different metal ions, namely Pb(II), Bi(III), Mg(II), Cu(II), and Zn(II), at the investigated dye's maximum emission wavelength of 398 nm, the fluorescence intensity of the ISoXD complex increases, as depicted in Fig. 10. Notably, the introduction of a similar 1×10^{-5} M concentration of mercury results in a new emission maximum at 420 nm, as demonstrated in Fig. 11.

In an aqueous solution, we investigated how the magnetic susceptibility (MS) of metal ions that form complexes with ISoXD impacts the fluorescence intensity. The results, shown in Table 4 and Fig. 12, indicate that a decrease in the MS of metal ions, added at similar concentrations, leads to an increase in fluorescence intensity due to complex formation with these metal ions. Specifically, the formed Cu(II), Bi(III), Mg(II), Zn(II), and Hg(II), complexes exhibit higher intensities compared to a pure ethanolic solution of the studied dye as shown in Fig. 10 [41].

2.6. Interaction of ISoXD with DNA

The mechanism of ISoXD binding to DNA has been investigated using the absorption spectra. By including various DNA concentrations with the examined molecule, the binding of ISoXD compound to DNA has been assessed. Fig. 13 displays the absorption spectra of the studied dye. The addition of DNA led to a clear change in the absorption spectra of ISoXD. A red shift (bathochromic) of 16 nm is observed from the absorption at 348 nm and the absorption intensity increase by 64.05% (hyperchromic effect). The typical characteristic of DNA intercalation is the augmentation in the intensity of the absorption peaks (hyperchromic effect) exhibited by small molecules. The evidence for ISoXD intercalation in DNA came from this hyperchromic effect. This suggests that the ISoXD chromophore of the DNA base pairs is quite close by, which means that there is a significant electronic state overlap between the intercalating

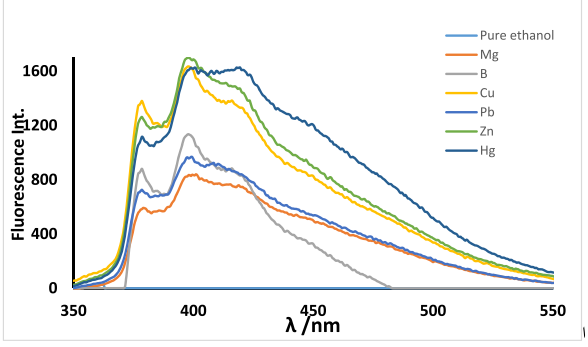

Fig. 10. Fluorescence spectra of 2×10^{-5} M ISoXD in pure ethanol and ethanol containing of 2×10^{-5} M of different metal ions, $\lambda_{ex} = 340$ nm.

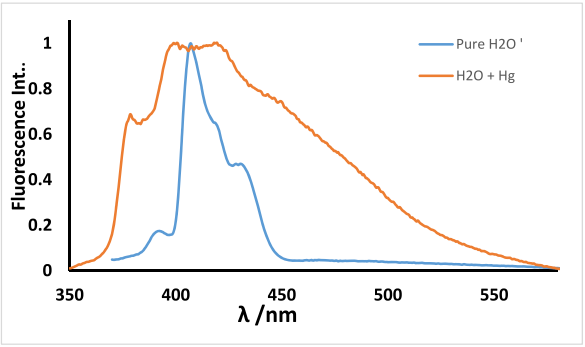

Fig. 11. Normalized fluorescence spectra of 1.04×10^{-4} M of ISoXD in pure H_2O and 2×10^{-5} M Hg^{2+}, $\lambda_{ex} = 350$ nm.

Table 4
Magnetic susceptibility of metals, and fluorescence intensities of the formed complex with ISoXD.

M^+	B	Cu	Hg	Mg	Pb	Zn
MS × $\chi_m/10^{-6}$ cm^3 mol^{-1}	−6.7	−5.46	−24.1	13	−10.2	−9.15
Emission Intensity	1130	1648	1626	831	951	1695

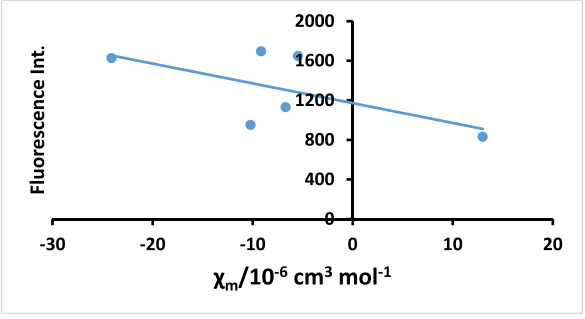

Fig. 12. A plot of fluorescence intensities of complexes with magnetic susceptibility values of different metal ions.

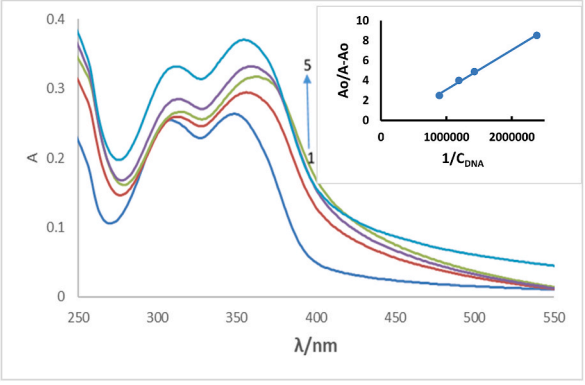

Fig. 13. UV–Vis absorption spectra of ISoXD (2×10^{-5} M) in the absence and presence of DNA. The concentration of DNA from 0 to 5 were 1) 0.0, (2) 4.2×10^{-7} M, (3) 7×10^{-7} M, (4) 8.4×10^{-7} M, (5) 11.2×10^{-7} M.

chromophore and the DNA bases [42].

To clarify the robustness of the interaction between ISoXD and DNA, the binding constant K_b was obtained. The binding constant was determined from the differences in absorbance (A) due to DNA intercalation using the following Benesi–Hildebrand equation [24, 42].

$$\frac{Ao}{A-Ao}=\frac{\varepsilon_G}{\varepsilon_{H-G}-\varepsilon_G}+\frac{\varepsilon_G}{\varepsilon_{H-G}-\varepsilon_G}\times\frac{1}{k_b}\frac{1}{C_{DNA}} \quad (1)$$

The plot of $A^0/A\text{-}A^0$ vs $1/C_{DNA}$ exhibits a high degree of linearity with regression coefficient 0.968 and was used to determine the K_b values from the slope and intercept. Based on this calculation, K value is equal to $2.18 \times 10^6\ M^{-1}$. The value of K_b is apparently close to that of the classic intercalation such as ethidium bromide -DNA complex ($K_b = 1.4 \times 10^6\ M^{-1}$) [43–45], pointing out that ISoXD binds to DNA through intercalation binding. The standard Gibbs free change ΔG^o, which indicates the degree of binding and the stability of the produced complex in the binding system of intercalations, can be computed using the following equation:

$$\Delta G^o = -RT \ln k_b \quad (2)$$

Where the R is the gas constant ($8.31\ J\ K^{-1}\ mol^{-1}$), T is the absolute temperature (298.15 k), K_b is the binding constant. The value of ΔG^o was discovered to be negative (−30.479 kJ/mol), demonstrating the favorable and spontaneous character of the binding process between ISoXD and DNA.

2.7. Host–guest interactions of ISoXD with β-CD

Absorption spectra were frequently utilized in the research of host-guest supramolecular chemistry to confirm the production of inclusion complexes (IC) [46]. UV–Visible spectroscopy was employed to confirm the formation of the inclusion complex of ISoXD-β-CD. The absorbance spectra of ISoXD showed an increment with the increase in the quantity of β-CD, but no shift in λ_{max} at 348 nm was observed (Fig. 14). The solute inclusion process alters the solvent's microenvironment, which is thought to be the cause of these variations in absorbance values. The loss of hydrogen bonding that occurs with the transfer of the guest molecule from the solution of the β -CD cavity may be the cause of the variations in molar absorptivity values.

Equation (1) was employed to calculate the binding constant by plotting the $A^0/A\text{-}A^0$ *vs.* $1/C_{\beta\text{-}CD}$ (Fig. 14). The calculated binding constant was $1.74 \times 10^3\ M^{-1}$. The standard Gibbs free energy was also calculated by equation (2) and the result is equal to −18.502 kJ/mol. This negative value means that the interaction between ISoXD and β-CD was favorable and spontaneous.

2.8. Molecular docking

The selection of Human PARP-1 enzyme was made using recommendations from the Swiss target prediction web site, from which the SMILES for ISoXD were submitted. due to a lack of knowledge regarding their binding in biological targets, we utilized the Swiss Target Prediction web service to predict potential protein targets. PARPs are a class of enzymes that catalyze the transfer of ADP-ribose from nicotinamide adenine dinucleotide (NAD+) to acceptor proteins and play an important role in DNA repair and cell death [47–49]. PARP-1 is the most studied member of this family, which has at least 15 members. It mainly acts as a DNA repair factor, particularly in base excision repair (BER). Because of its synthetic lethal interaction with breast cancer susceptibility proteins 1 and 2, PARP1 is a particularly significant therapeutic target for the treatment of breast cancer.

Inhibitors of this enzyme are a novel kind of anticancer medication that kills cancer cells selectively by targeting homologous recombination repair faults. PARP inhibitors are one of the most effective innovative methods to cancer therapy. Indeed, PARP inhibitors have recently been granted by the US Food and Drug Administration (FDA) for the treatment of breast and ovarian malignancies. PARP-1 inhibitors were thought to impede PARP-1 enzymatic activity and hinder BER-mediated DNA single-strand break (SSB) repair, resulting in cell death via a synthetic lethality mechanism and anticancer effects [47,48].

The docking analysis of ISoXD in the PARP-1 binding cavity (PDB ID: 7KK6) reveals docking scores and MM-GBSA binding free energies of −6.511 and −66.27 kcal/mol, respectively, while the co-crystal PARP-1 inhibitor veliparib displays −8.224 and −57.9 kcal/mol. Maestro's ligand-interaction tool was used to create the 2D and 3D graphical representations of the ISoXD-protein interactions shown in Fig. 15. The ISoXD binding interaction is completely compatible with that of the co-crystal ligand veliparib, which targets the nicotinamide-binding pocket. The formed complex ISoXD-PARP-1 was highly stabilized by two conventional H-bonds together with two π-π interactions. Two H-bonds were generated, by the phenolic hydroxyl group with Glu988 at 2.09 Å and Tyr907 at 2.012 Å amino acids. The two π-π interactions were formed between the phenyl ring of the central phenol moiety with Tyr896 at 2.30 Å

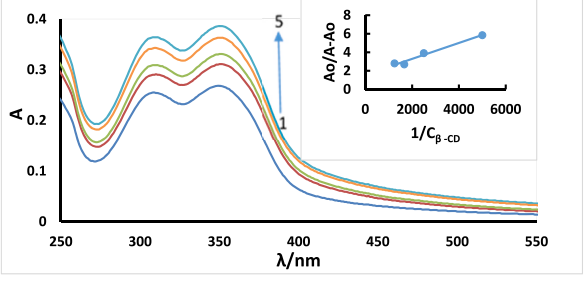

Fig. 14. UV–Vis absorption spectra of ISoXD (2×10^{-5} M) in the absence and presence of β-CD. The concentration of β-CD from 0 to 5 were 1) 0.0, (2) 2×10^{-4} M, (3) 4×10^{-4} M, (4) 6×10^{-4} M, (5) 8×10^{-4} M.

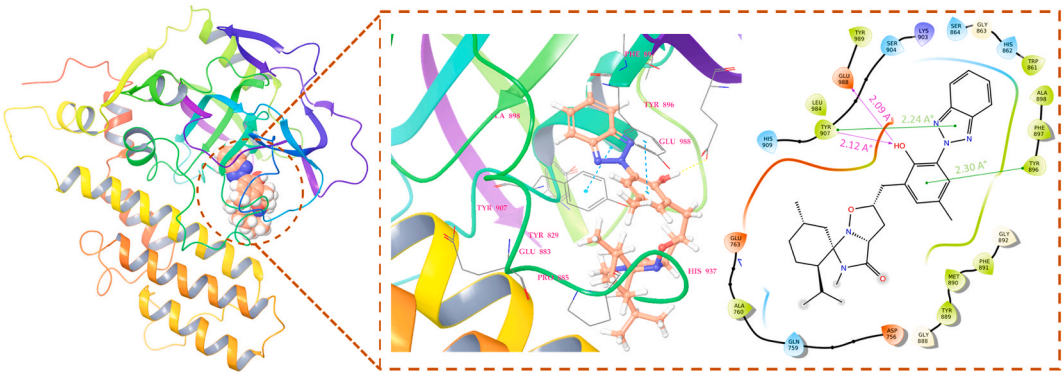

Fig. 15. 2D and 3D Binding interaction of ISoXD in the PARP-1 binding cavity (PDB ID: 7KK6).

and Benzotriazole and Tyr907 at 2.24 Å. According to reports, the amide groups present in Niraparib and veliparib, as well as the pyridazinone moiety found in Talazoparib and Olaparib, are similar to the amide group in nicotinamide. Inhibitors of the PARP1 enzyme bind to Tyr907 and form hydrogen bonds with the backbone nitrogen and carbonyl oxygen of Gly863, as well as the sidechain hydroxyl of Ser904 [50]. Therefore, the comparable binding affinity and interaction of ISoXD with the key residue Tyr907 suggest that it has anticancer properties through the inhibition of the PARP-1 enzyme.

2.9. MD simulation

The PARP-1 docked complex with ISoXD was subjected to a simulation study for 100 ns to analyze the stability in the binding region of the PARP-1 enzyme. The RMSD measurements were used to assess the stability of the docking positions. The RMSD value indicates structural variation and protein stability [51,52]. As can be seen from Fig. 16A. The RMSD for the PARP-1 protein Cα atoms is 1.50–2.27 Å for the 100 ns simulation runtime. The RMSD value of ISoXD is 1.6–3.6 Å and the average value is 2.9 Å, resulting in stable fluctuations through the runtime of the 100 ns simulation. The low RMSD of protein and ligand, as well as no significant shifts in the graph, suggest that ISoXD remained stable in the PARP-1 binding cavity over the 100-ns simulation.

The root-mean-square fluctuations (RMSF) is crucial for protein characterization [53–55]. Throughout the simulation, significant alterations were seen at the N-terminal which is protein flexible region. High fluctuation is observed in residues with Ser661 (3.62 Å) and Gly723 (3.77 Å), which are not involved in ligand interaction. During the simulation ISoXD interacted with 16 amino acids of PARP-1 protein including Asp756 (1.0 Å), Gln759 (0.6 Å), Ala760 (0.7 Å), His862 (0.4 Å), Gly863 (0.6 Å), Ser864 (0.6 Å), Gly888 (1.2 Å), Tyr889 (0.7 Å), Met890 (0.7 Å), Tyr896 (0.5 Å), Phe897(0.4 Å), Ala898 (0.5 Å), Lys903 (0.5 Å), Asn906 (0.6 Å), Tyr907 (0.6 Å), and Glu988 (0.5 Å). All these interacted is highlighted with green color vertical bar. The conformational changes of essential amino acids in the PARP-1 binding cavity (lowest RMSF value) demonstrated the ISoXD capacity to generate stable interactions with the PARP-1 protein Fig. 16B. Protein interactions with the ligand may be seen throughout the 100 ns simulation. Figs. 16C and D depicts how these interactions might be classified and summarized by type. The inquiry revealed four kinds of protein-ligand interactions (or "contacts"): hydrogen bonds, hydrophobic interactions, ionic interactions, and water bridges. The SID module was utilized for examining the subcategories of each interaction type [56,57]. Along the trajectory, the stacked bar charts are normalized: a value of 0.8 indicates that the particular contact is maintained for 80% of the simulation time. ISoXD exhibited strong hydrogen bond interactions with different amino acids such as Tyr907 and Glu988 with 65% and 97% of simulation time, respectively. In the case of hydrophobic interaction, the amino acids Tyr896 and Tyr907 interacted more significantly with a percentage of 94% and 72%, respectively. Hydrogen bonding and hydrophobic interactions were the main ligand-protein interactions identified during 100 ns MD simulation. It is highlighted that the current study provides in silico predictions and simulations and further experimental work, such as biological assays, is imperative to validate the actual impact of the compounds on the predicted targets in a biological context.

2.10. DFT

Theoretical computations in DFT and time-dependent density functional theory (TDDFT) were carried out using the Gaussian09 program [58] to investigate the electronic characteristics of the ligand alone, and the ligand and Hg^{2+} forming a compound. These electronic characteristics contribute to fluorescence quenching. To optimize the various structures, the basis sets 6-31G(d)/Lanl2dz and PBE1PBE functional were employed. The LANL2DZ basis set was used for all Hg atoms, while 6-31G(d) was used for all other atoms. All calculations included the solvation model SMD and water. To demonstrate the complex stability of the ligand and the complex, we performed frequency calculations with the same functional and basis set. The selection of the particular basis set and DFT functional was determined through comprehensive calculations, as documented in a prior study [23], which investigated analogous systems and examined the same property. This property encompasses quenching in the presence of Hg^{2+} and an organic system, demonstrating concurrence with experimental results.

We used the optimized structures to run TDDFT calculations with the solvation model SMD (water) at the PBE1PBE/aug-cc-

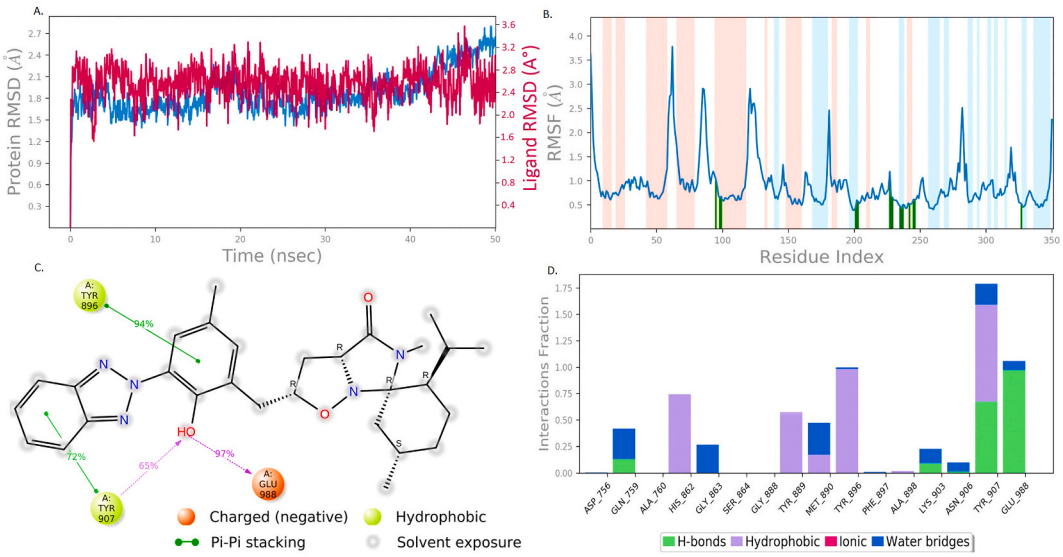

Fig. 16. MD simulation analysis of compound ISoXD in the PARP-1 binding cavity (PDB ID: 7KK6), A: RMSD (Protein RMSD is shown in blue while RMSD of compound Prunetin are shown in red), B: Protein RMSF, C: 2d Interaction diagram and D: Protein–ligand contact analysis of MD trajectory. (For interpretation of the references to color in this figure legend, the reader is referred to the Web version of this article.)

pVDZPP/6-31+G(d) level of theory. The corresponding effective core potentials (ECP) and Dunning's double zeta augmented correlation consistent polarized basis set (aug-cc-pVDZPP) were used for Hg [59,60]. Fig. 17 depicts the optimal structures of the ligand alone L, the and the Hg^{2+} complex (Hg^{2+}- L) using solvation model SMD (water).

Fig. 17 shows that Hg^{2+} can have interactions with the ligand's two oxygen and two nitrogens, (Hg^{2+}-L). We propose that this structure can be used as a model. It is similar to the reference model [23].

The possible transitions for the most stable structures were computed using TDDFT. Fig. 18 depicts chosen molecular orbitals of L and Hg^{2+}-L. Table 5 contains TDDFT results concerning wavelength, electronic transitions, and oscillator strength. The aromatic rings in the L molecule have the highest density of electrons in the different frontier orbitals. The transition (HOMO to LUMO) in Hg^{2+}-L allows for ICT: the density of electrons present in the HOMO is primarily distributed on aromatic rings of the ligand L, whereas the density of electrons in the LUMO is primarily distributed on the metal Hg. As a result, the ICT from the L molecule to Hg(II) helps to quench the fluorescence probe. The small value of the oscillator strength supports these findings (Table 5).

3. Materials and methods

3.1. Synthesis of compound 2

To a solution of **1** (1 eq.) in toluene was added 2-allyl-6-benzotriazol-2-yl-4-methyl-phenol (1 eq.). The mixture was refluxed for 72h with stirring. The obtained cycloadduct was purified by flash chromatography (Cyclohexane/EtOAc 7:3) to separate the desired compound **2**.

(1S,2S,2′R,3a′R,5R)-2'-(3-(2H-benzo[d] [1–3]triazol-2-yl)-2-hydroxy-5-methylbenzyl)-2-isopropyl-5,5′-dimethyldihydro-2′H-spiro [cyclohexane-1,6′-imidazo [1,5-b]isoxazol]-4′(5′H)-one.

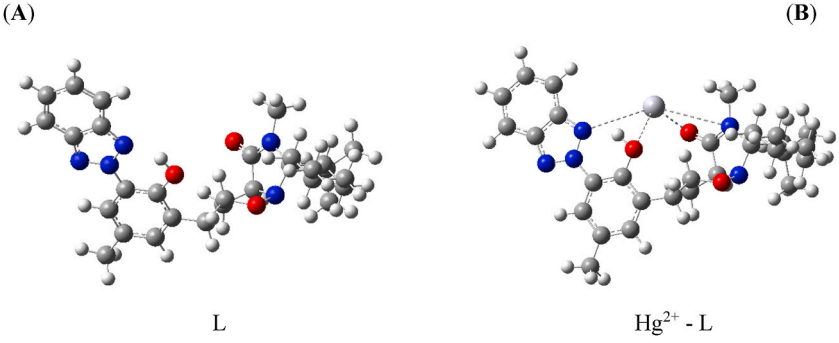

Fig. 17. Models optimized by DFT using solvation model SMD and water for (A) Ligand L and (B) complexes Hg^{2+}-L.

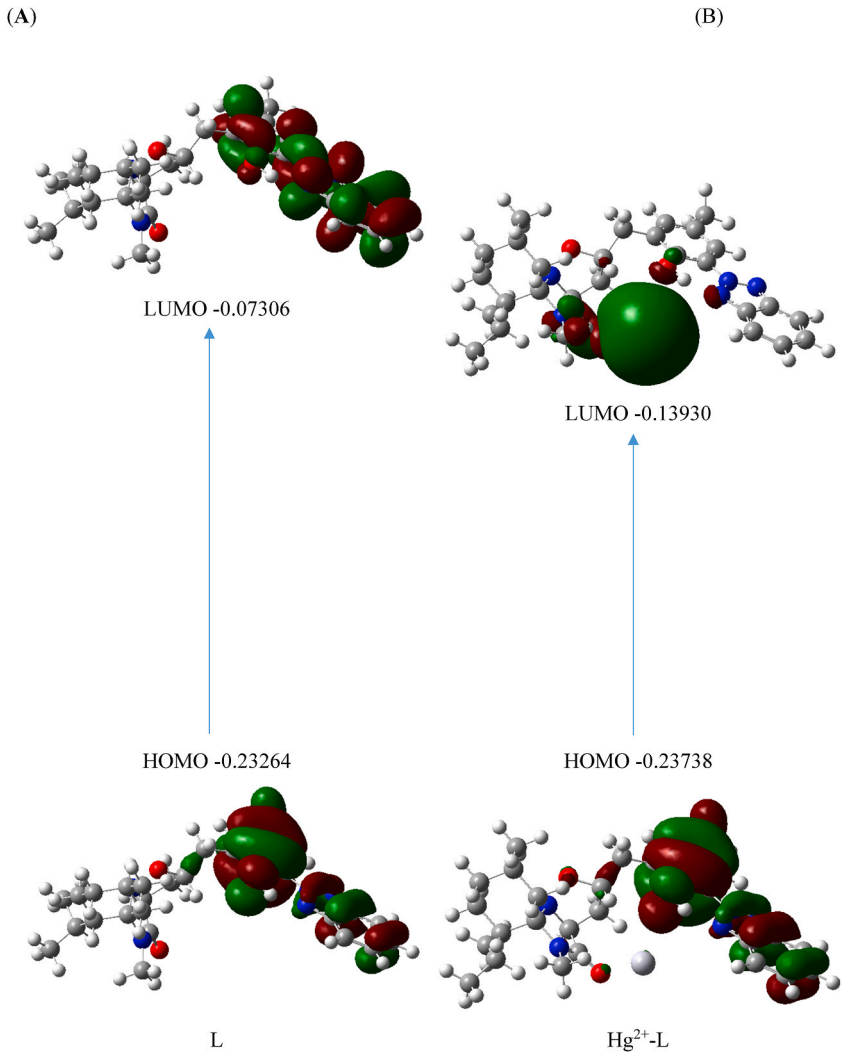

Fig. 18. Frontier orbitals and their energies for (A) L and (B) Hg^{2+}-L.

Table 5
The TDDFT results of selected electronic transitions, absorption energies and oscillator strengths.

Complex	Transition	λ(nm)	Oscillator Strength
L	HOMO → LUMO	344	0.4271
Hg^{2+}-L	HOMO→ LUMO	639	0.0403

1H NMR ($CDCl_3$, 400 MHz) 0.68 (d, 3H, $J = 7.2$ Hz, CH_3); 0.83 (d, 3H, $J = 6.8$ Hz, CH_3); 0.86 (d, 3H, $J = 6.8$ Hz, CH_3); 0.87–0.92 (m, 1H); 1.11 (t, 1H, $J = 12.4$ Hz); 1.30 (dd, 1H, J = 2.0 and 11.6 Hz); 1.40 (quin, 1H, $J = 6.8$ Hz); 1.58–1.62 (m, 1H); 1.69–1.79 (m, 3H); 1.91–1.98 (m, 1H); 2.28 (ddd, 1H, J = 2.8, 9.2 and 12 Hz); 2.34 (s, 3H, CH_3); 2.67 (s, 3H, NCH_3); 2.68–2.73 (ddd, 1H, J = 3.6, 8.8 and 12 Hz); 2.83 (dd, 1H, J = 8.4 and 13.6 Hz); 3.18 (dd, 1H J = 4.4 and 13.6 Hz); 4.00 (d, 1H, $J = 8.8$ Hz, H-3); 4.07–4.12 (m, 1H, H-5); 7.10 (s, 1H); 7.46 (d, 1H, $J = 3.2$ Hz); 7.48 (d, 1H, $J = 2.8$ Hz); 7.91 (d, 1H, $J = 2.8$ Hz); 7.93 (d, 1H, $J = 3.2$ Hz); 8.08 (d, 1H, $J = 1.2$ Hz); 11.31 (s, 1H, OH).

13C NMR ($CDCl_3$, 100 MHz) 14.2; 18.4; 20.5; 21.0; 22.0; 22.3; 24.1; 24.3; 25.9; 29.6; 33.1; 34.6; 38.7; 40.4(C4); 48.1(C8); 60.3; 66.3(C3); 76.5(C7); 89.7(C5); 117.6; 119.6; 124.7; 127.6; 127.8; 128.7; 132.9; 142.7; 145.4; 172.9 (C═O).

Anal. Calcd. for $C_{29}H_{37}N_5O_3$ (503.65): C, 69.16; H, 7.41; N, 13.91, Found: C, 68.93; H, 7.33; N, 13.82.

3.2. UV–Vis. and fluorescence spectra

The spectral characteristics of the compound (UV–Vis absorption spectra) was measured using a Shimadzu spectrophotometer

(UV–1650PC, Japan) using 1 cm quartz cell. The wavelength range used was 200–800 nm. A Jasco FP-8200 spectrometer was also used to measure the steady-state fluorescence of 4nmn dye in different media. All solvents used are of spectroscopic grade.

3.3. Photochemical quantum yield

Using a modified A. J. Lees method that takes into consideration the decrease in absorbance at the excitation wavelength as photoirradiation time increases, photochemical quantum yields of 4NMN (ϕ_c) were measured [60].

3.4. Fluorescence quantum yield

The determination of the fluorescence efficiency was done using either quinine sulfate or 9,10-diphenyle anthracene solutions, depending on the emission wavelength range. The light intensity was measured using ferrioxalate actinometry [34,61]. The fluorescence quantum yields were calculated utilizing equation (3).

$$\varnothing_f(s) = \varnothing_f(r) \times \frac{\int I_s}{\int I_r} \times \frac{A_r}{A_s} \times \frac{n_s^2}{n_r^2} \quad (3)$$

The corrected fluorescence peak areas are denoted as the integrals, A is absorbance at excitation wave length, and n is the refractive index of the solvent. Sample and reference are denoted by the subscripts s and r, respectively.

3.5. DNA and β-CD binding studies

Salmon double strand deoxyribonucleic acid (DNA) and β-Cyclodextrin (β-CD) were obtained from Sigma and used without further purification. A stock solution of DNA and β-CD were prepared by dissolving them in deionized water. The DNA stock solution was measured by UV at an absorbance of 260 nm using a molar extinction coefficient (ε) of 6600 $M^{-1}cm^{-1}$. The absence of protein in the DNA was confirmed by studying the ratio $A_{260}/A_{280} = 1.89$ (over 1.8) [24,62]. A Britton-Robinson (BR) buffer was prepared by mixing 0.04 M boric acid, 0.04 M orthophosphoric acid, and 0.04 M acetic acid, which was adjusted to pH 7.4 by adding an appropriate amount of 0.2 M sodium hydroxide [42]. All chemicals were reagent-grade (Sigma, USA). All experiments of the ISoXD compound with DNA and β-CD were carried out in BR buffer at pH 7.4.

3.6. Molecular docking and Molecular dynamic (MD) simulation

Molecular docking study were performed on the structure of the catalytic domain of Poly(ADP-ribose) polymerase-1 (PARP-1) in association with veliparib (PDB ID: 7KK6) as a target enzyme. Based on structure activity relationship (SAR) investigation, the target protein was identified utilizing a Swiss target prediction web service (http://www.swissadme.ch), by submitting SMILES of ISoXD. The docking was carried out in the active site of a receptor protein utilizing the SP (standard precision) Glide simulation-based docking technology, using the same ligand preparation, protein preparation, and grid box generating steps as previously described [16]. The Desmond package was used to run MD simulations on the OPLS3e force field. To account for long-range electrostatic interactions, the smooth particle mesh Ewald approach with a tolerance of 1e-09 was employed. Additionally, short-range Van der Waals and Coulomb interactions were considered using a cut-off radius of 9.0 Å. Subsequently, a 100 ns MD simulation was performed under an "isothermal-isobaric ensemble" (NPT) at a temperature of 300 K and a pressure of 1 bar. The thermostat and barostat techniques, specifically "Nose-Hoover chain thermostat" and "Martyna-Tobias-Klein barostat," were applied for isothermal-isobaric conditions at intervals of 100 and 200 ps, respectively. Throughout the simulation, snapshots were taken at 100 ps intervals, and the resulting trajectories were analyzed [16]. Molecular Mechanics/Generalized Born Surface Area (MM/GBSA) method was used to obtain the binding free energy of the interaction between ligand-protein complexes. The simulation lasted 100 ns, and trajectory snapshots were obtained every 100 ps. Desmond's Simulation Interaction Diagram (SID) was utilized to project the ligand's binding orientation and stability.

4. Conclusion

In the present study, a novel ISoXD was synthesized and evaluated for their optical properties. It has been noted that the blue shift in absorption spectra of ISoXD, in water to 340 compared to that in ethanol solvents, which is attributed to the hydrogen bonding interaction. A more pronounced effect was observed in the excited state. A Stokes shift was detected for the studied compound in different solvents. An internal filter effect was also observed indicating that using a higher concentration of ISoXD is not preferable. It was mentioned that the fluorescence intensity of the ISoXD complex increased in ethanol with the addition of Pb (II), Ni (II), Mn (II), Cu (II), and Zn (II). The appearance of a new maximum emission wavelength at 420 nm with the addition of a small amount of mercury ions encourages its use as a probe to determine trace amounts of mercury. The Hg (II) complex geometry and its electronic structure were studied using DFT and TDDFT. The study shows an ICT mechanism which contributes to the quenching property. ISoXD binds to DNA through intercalation, exhibiting a strong binding affinity (2.18×10^6 M^{-1}) and a favorable and spontaneous binding process. The calculated binding constant between ISoXD and β-CD was found to be 1.74×10^3 M^{-1}, indicating a relatively weak interaction. However, the binding is still favorable and spontaneous based on the calculated standard Gibbs free energy value (−18.502 kJ/mol). In

this study, we conducted a docking analysis of ISoXD within the PARP-1 binding cavity. Our analysis yielded impressive results, with ISoXD showing docking scores and MM-GBSA binding free energies of −6.511 and −66.27 kcal/mol, respectively. Notably, ISoXD's binding interaction closely resembles to that of the co-crystal ligand veliparib, which specifically targets the nicotinamide-binding pocket. To further investigate ISoXD's potential, we subjected it to a 100ns MD simulation. Throughout this simulation, ISoXD demonstrated remarkable stability and formed strong hydrogen bond interactions with key amino acids, including Tyr907 and Glu988. These findings suggest that ISoXD holds significant promise as a candidate for PARP-1 inhibition and merit further exploration in the development of novel therapies.

CRediT authorship contribution statement

Afnan Alotayeq: Software, Resources, Investigation. **Siwar Ghannay:** Writing – original draft, Resources, Methodology, Conceptualization. **Ibrahim A. Alhagri:** Writing – review & editing, Writing – original draft, Methodology, Investigation, Formal analysis, Conceptualization. **Iqrar Ahmed:** Writing – original draft, Software, Methodology, Data curation. **Bechir Hammami:** Software, Resources. **Abuzar E. A. E. Albadri:** Resources, Formal analysis. **Harun Patel:** Writing – original draft, Software. **Sabri Messaoudi:** Writing – review & editing, Writing – original draft, Visualization, Software, Data curation. **Adel Kadri:** Writing – review & editing, Visualization, Validation, Supervision. **Sadeq M. Al-Hazmy:** Writing – review & editing, Writing – original draft, Visualization, Supervision, Methodology, Conceptualization. **Kaiss Aouadi:** Writing – review & editing, Writing – original draft, Visualization, Validation, Conceptualization.

Declaration of competing interest

The authors declare that they have no known competing financial interests or personal relationships that could have appeared to influence the work reported in this paper.

Appendix A. Supplementary data

Supplementary data to this article can be found online at https://doi.org/10.1016/j.heliyon.2024.e26341.

References

[1] S.D. Karyakarte, T.P. Smith, S.R. Chemler, Stereoselective isoxazolidine synthesis via Copper-catalyzed alkene aminooxygenation, J. Org. Chem. 77 (2012) 7755–7760.
[2] D.G. Piotrowska, I.E. Głowacka, D. Schols, R. Snoeck, G. Andrei, J. Gotkowska, Novel isoxazolidine and γ-lactam analogues of homonucleosides, Molecules 24 (2019) 4014.
[3] D.G. Piotrowska, G. Andrei, D. Schols, R. Snoeck, M. Grabkowska-Drużyc, New isoxazolidine-conjugates of quinazolinones—synthesis, antiviral and cytostatic activity, Molecules 21 (2016) 959.
[4] D.D. Karcev, M.M. Efremova, A.P. Molchanov, N.V. Rostovskii, M.A. Kryukova, A.S. Bunev, D.A. Khochenkov, Selective and reversible 1,3-dipolar cycloaddition of 2-(2-Oxoindoline-3-ylidene)acetates with nitrones in the synthesis of functionalized spiroisoxazolidines, Int. J. Mol. Sci. 23 (2022) 12639.
[5] K. Aouadi, S. Vidal, M. Msaddek, J.P. Praly, Stereoselective synthesis of 1,2,3-triazolyl-functionalized isoxazolidines, via two consecutive 1,3-dipolar cycloadditions, as precursors of unnatural amino acids, Tetrahedron Lett. 54 (2013) 1967–1971.
[6] M. Berthet, T. Cheviet, G. Dujardin, I. Parrot, J. Martinez, Isoxazolidine: a privileged scaffold for organic and medicinal chemistry, Chem. Rev. 116 (2016) 15235–15283.
[7] X. Li, P. Zhai, Y. Fang, W. Li, H. Chang, W. Gao, Synthesis of isoxazolidines via catalyst-free one-pot three-component cycloaddition of sulfoxonium ylides, nitrosoarenes and alkenes, Org. Chem. Front. 8 (2021) 988–995.
[8] A. Al-Adhreai, M. Alsaeedy, A. Alrabie, I. Al-Qadsy, S. Dawbaa, Z.M. Alaizeri, H.A. Alhadlaq, A. Al-Kubati, M. Ahamed, M. Farooqui, Design and synthesis of novel enantiopure Bis(5-Isoxazolidine) derivatives: insights into their antioxidant and antimicrobial potential via in silico drug-likeness, pharmacokinetic, medicinal chemistry properties, and molecular docking studies, Heliyon 8 (2022) e09746.
[9] A.I. Said, T.I. El-Emarya, Diastereoselective synthesis of atropisomeric pyrazolyl pyrrolo[3,4-d]isoxazolidines via pyrazolyl nitrone cycloaddition to facially divergent maleimides: intensive NMR and DFT studies, RSC Adv. 10 (2020) 845–850.
[10] C. Kouklowsky, The pivotal role of N-O bonds in the synthesis of natural products: a mini-review, Vietnam J. Chem. 58 (2020) 20–28.
[11] E.M. Tsyrlina, T.M. Gabbasov, A.N. Lobov, et al., Synthetic transformations of the isoxazolidine ring of lappaconitine derivatives, Chem. Nat. Compd. 58 (2022) 784–787.
[12] S. Ghannay, S. Bakari, M. Msaddek, S. Vidal, A. Kadri, K. Aouadi, Design, synthesis, molecular properties and in vitro antioxidant and antibacterial potential of novel enantiopure isoxazolidine derivatives, Arab. J. Chem. 13 (2020) 2121–2131.
[13] J. Brahmi, S. Ghannay, S. Bakari, K. Aouadi, A. Kadri, M. Msaddek, S. Vidal, Unprecedented stereoselective synthesis of 3-methylisoxazolidine-5-Aryl-1,2,4-Oxadiazoles via 1,3-Dipolar cycloaddition and study of their in vitro antioxidant activity, Synth. Commun. (2016) 2037–2044.
[14] S. Ghannay, M. Snoussi, S. Messaoudi, A. Kadri, K. Aouadi, Novel enantiopure isoxazolidine and C-Alkyl imine oxide derivatives as potential hypoglycemic agents: design, synthesis, dual inhibitors of α-amylase and α-Glucosidase, ADMET and molecular docking study, Bioorg. Chem. 104 (2020) 104270.
[15] A. Ghabi, J. Brahmi, F. Alminderej, S. Messaoudi, S. Vidal, A. Kadri, K. Aouadi, Multifunctional isoxazolidine derivatives as α-amylase and α-glucosidase inhibitors, Bioorg. Chem. 98 (2020) 103713.
[16] F. Alminderej, S. Ghannay, M. Omer Elsamani, F. Alhawday, A.E.A.E. Albadri, S.E.I. Elbehairi, M.Y. Alfaifi, A. Kadri, K. Aouadi, In vitro and in silico evaluation of antiproliferative activity of new isoxazolidine derivatives targeting EGFR: design, synthesis, cell cycle analysis, and apoptotic inducers, Pharmaceuticals 16 (2023) 1025.
[17] K. Aouadi, S. Vidal, M. Msaddek, J.P. Praly, Cycloadditions of chiral nitrones to racemic 3-substituted butenes: a direct access with kinetic resolution to enantiopure dihydroxylated amino acids, Synlett 19 (2006) 3299–3303.
[18] K. Aouadi, E. Jeanneau, M. Msaddek, J.P. Praly, New synthetic routes toward enantiopure (2S,3R,4R)-4-Hydroxyisoleucine by 1,3-dipolar cycloaddition of a chiral nitrone to C4 alkenes, Synthesis 21 (2007) 3399–3405.

[19] J. Al-Harby, H. Tar, S.M. Al-Hazmy, Photoinduced and classical sol-gel synthesis: spectral and photophysical behavior of silica matrix doped by novel fluorescent dye based on boron difluoride complex, Polymers 13 (2021) 2743.
[20] S.M. Al-Hazmy, M.O. Zouaghi, J.N. Al-Johani, Y. Arfaoui, R. Al-Ashwal, B. Hammami, I.A. Alhagri, N.A. Alhemiary, N. Handi, Chemosensing properties of coumarin derivatives: promising agents with diverse pharmacological properties, docking and DFT investigation, Molecules 27 (2022) 1–31.
[21] S.M. Al-Hazmy, Y. El-Ghoul, J. Al-Harby, H. Tar, F.M. Alminderej, Synthesis, characterization, and performance of pyridomethene-BF2 fluorescence dye-doped PVA thin film and PVP nanofibers as low γ-ray dosimeters, ACS Omega 7 (2022) 34002–34011.
[22] L.F. Minuti, M.G. Memeo, S. Crespi, P. Quadrelli, Fluorescent probes from stable aromatic nitrile oxides, Eur. J. Org. Chem. 2016 (2016) 821–829.
[23] R. Ali, S. Ghannay, S. Messaoudi, F.M. Alminderej, K. Aouadi, S.M. Saleh, A reversible optical sensor film for mercury ions discrimination based on isoxazolidine derivative and exhibiting pH sensing, Biosensors 12 (2022) 1028.
[24] M. Sirajuddin, S. Ali, A. Badshah, Drug-DNA interactions and their study by UV-visible, fluorescence spectroscopies and cyclic voltametry, J. Photochem. Photobiol., B 124 (2013) 1–19.
[25] G. Magdy, M.A. Shaldam, F. Belal, H. Elmansi, Multi-spectroscopic, thermodynamic, and molecular docking/dynamic approaches for characterization of the binding interaction between calf thymus DNA and palbociclib, Sci. Rep. 12 (2022) 1–13.
[26] Y. Sun, S. Bi, D. Song, C. Qiao, D. Mu, H. Zhang, Study on the interaction mechanism between DNA and the main active components in scutellaria baicalensis georgi, Sens Actuators B Chem 129 (2008) 799–810.
[27] N. Bensouilah, M. Abdaoui, Inclusion complex of N-nitroso, N-(2-Chloroethyl), N′, N′-Dibenzylsulfamid with β-cyclodextrin: fluorescence and molecular modeling, C. R. Chim. 15 (2012) 1022–1036.
[28] Z. Fülöp, S.V. Kurkov, T.T. Nielsen, K.L. Larsen, T. Loftsson, Self-assembly of cyclodextrins: formation of cyclodextrin polymer based nanoparticles, J. Drug Deliv. Sci. Technol. (2012) 215–221. Editions de Sante.
[29] D. Boczar, K. Michalska, Cyclodextrin inclusion complexes with antibiotics and antibacterial agents as drug-delivery systems—a pharmaceutical perspective, Pharmaceutics 14 (2022) 389.
[30] Svenja Wüpper, Kai Lüersen, G. R, Cyclodextrins, natural compounds, and plant bioactives—a nutritional perspective, Biomolecules 11 (2021) 401.
[31] S. Chakraborty, P. Ghosh, B. Basu, A. Mandal, Inclusion complex of β-cyclodextrin with tetrabutylammonium bromide: synthesis, characterization and interaction with calf thymus DNA, J. Mol. Liq. 293 (2019) 111525.
[32] S. Kim, T.G. Hwang, J.W. Namgoong, H.M. Kim, J.P. Kim, Effect of linker moiety on linear dimeric benzotriazole derivatives as highly stable UV absorber for transparent polyimide film, Dyes Pigments 180 (2020) 108469.
[33] S. Naumov, B. Herzog, B. Abel, Spectra and photorelaxation of hydroxyphenyl-benzotriazole-type UV absorbers: from monomers to nanoparticles, J. Phys.l Chem. A 124 (2020) 625–632.
[34] A. Mnasri, A. Mejri, S.M. Al-Hazmy, Y. Arfaoui, I. Özdemir, N. Gürbüz, N. Handi, Silver–N-Heterocyclic carbene complexes-catalyzed multicomponent reactions: synthesis, spectroscopic characterization, density functional theory calculations, and antibacterial study, Arch. Pharm. 354 (2021) 2100111.
[35] I. Slimani, N. Hadi, S.M. Al-Hazmy, I.A. Alhagri, E.Z.M. Ebeid, E.A. Okba, Synthesis and spectral characterisation of (E)-3-(3-(4 (Dimethylaminesno)Phenyl) Acrylo-Yl)-4-Hydroxy-2H-Chromen-2-One and their antibacterial activity and acetylcholiterase inhibition, J. Chem. 2021 (2021). ID 6101359.
[36] A.N. Al-romaizan, M.A. Hussein, A new candidate laser dye based 1,4-Bis[β-(2-Naphthothiazolyle)Vinyl]Benzene. Spectroscopic behavior, laser parameters and excitation energy transfer, J. Fluoresc. 28 (2018) 743–758.
[37] P. Hrdlovic, J. Donovalova, H. Stankovicova, A. Gaplovsky, Influence of polarity of solvents on the spectral properties of bichromophoric coumarins, Molecules 15 (2010) 8915–8932.
[38] M. Makhloufi-Chebli, S.M. Hamdi, A. Rabahi, A.M.S. Silva, M. Handi, Estimation of ground- and excited-state dipole moments of 3-acetoacetyl-coumarin derivatives from a solvatochromic shift method based on the solvent polarity parameter, J. Mol. Liq. 181 (2013) 89–96.
[39] S.A. El-Daly, M. Gaber, S.S. Al-Shihry, Y.S.E. Sayed, Photophysical properties, excitation energy transfer and laser activity of 3-(4′-dimethylaminophenyl)-1-(2-Pyridinyl) Prop-2-En-1-one (DMAPP). A new potential laser dye, J. Photochem. Photobiol. Chem. 195 (2008) 89–98.
[40] J.R. Albani, Fluorescence: principles and observables, in: Principles and Observables, Structure and Dynamics of Macromolecules, 2004, pp. 55–98.
[41] D.R. Lide, Magnetic susceptibility of the elements and inorganic compounds, in: Handbook of Chemistry and Physics vol. 81, CRC Press, Boca Raton, Fla, 2000, pp. 130–135.
[42] I.A. Alhagri, Y.M. Temerk, S. M. Al Hazmy, M.M. Kamal, Binding of some antibacterial fluoroquinolones with Ds-DNA, β-cyclodextrin and hemoglobin : spectroscopic and voltammetric studies, Journal of Natural Sciences and Mathematics Qassim University 13 (2020) 24–41.
[43] J. Olmsted, D.R. Kearns, Mechanism of ethidium bromide fluorescence enhancement on binding to nucleic acids, Biochemistry 16 (1977) 3647–3654.
[44] M.J. Waring, Complex Formation between ethidium bromide and nucleic acids, J. Mol. Biol. 13 (1965) 269–282.
[45] G. Magdy, F. Belal, A.F. Abdel Hakiem, A.M. Abdel-Megied, Salmon sperm DNA binding study to cabozantinib, a tyrosine kinase inhibitor: multi-spectroscopic and molecular docking approaches, Int. J. Biol. Macromol. 182 (2021) 1852–1862.
[46] S. Chandrasekaran, Y. Sameena, I.V.M.V. Enoch, Modulation of the interaction of coumarin 7 with DNA by β-cyclodextrin, J. Inclusion Phenom. Macrocycl. Chem. 81 (2015) 225–236.
[47] S.A. Jannetti, B.M. Zeglis, M.R. Zalutsky, T. Reiner, Poly(ADP-Ribose)Polymerase (PARP) inhibitors and radiation therapy, Front. Pharmacol. 11 (2020) 1–14.
[48] Y.-Q. Wang, P.-Y. Wang, Y.-T. Wang, G.-F. Yang, A. Zhang, Z.-H. Miao, An update on Poly(ADP-Ribose)Polymerase-1 (PARP-1) inhibitors: opportunities and challenges in cancer therapy, J. Med. Chem. 59 (2016) 9575–9598.
[49] R.S. Cheke, V.M. Patil, S.D. Firke, J.P. Ambhore, I.A. Ansari, H.M. Patel, S.D. Shinde, V.R. Pasupuleti, M.I. Hassan, M. Adnan, et al., Therapeutic outcomes of isatin and its derivatives against multiple diseases: recent developments in drug discovery, Pharmaceuticals 15 (2022) 272.
[50] K. Ryan, B. Bolanos, M. Smith, P.B. Palde, P. Delgado Cuenca, T.L. VanArsdale, K.S. Gajiwala, Dissecting the molecular determinants of clinical PARP1 inhibitor selectivity for Tankyrase1, J. Med. Chem. 61 (2018) 1013–1020.
[51] I.M.M.M. Othman, H. Mahross, M.A.M. Gad-Elkareem, M. Rudrapal, N. Gogoi, D. Chetia, K. Aouadi, M. Snoussi, A. Kadri, Toward a treatment of antibacterial and antifungal infections: design, synthesis and in vitro activity of novel arylhydrazothiazolylsulfonamides analogues and their insight of DFT, docking and molecular dynamic simulations, J. Mol. Struct. 1243 (2021) 130862.
[52] H.A. Radwan, I. Ahmad, I.M.M. Othman, M.A.M. Gad-Elkareem, H. Patel, K. Aouadi, M. Snoussi, A. Kadri, Design, synthesis, in vitro anticancer and antimicrobial evaluation, SAR analysis, molecular docking and dynamic simulation of new pyrazoles, triazoles and pyridazines based isoxazole, J. Mol. Struct. 1264 (2022) 133312.
[53] J. Farmer, F. Kanwal, N. Nikulsin, M.C.B. Tsilimigras, D.J. Jacobs, Statistical measures to quantify similarity between molecular dynamics simulation trajectories, Entropy 19 (2017) 646.
[54] S. Rampogu, G. Lee, J.S. Park, K.W. Lee, M.O. Kim, Molecular docking and molecular dynamics simulations discover curcumin analogue as a plausible dual inhibitor for SARS-CoV-2, Int. J. Mol. Sci. 23 (2022) 1771.
[55] M.K. El-Ashrey, R.O. Bakr, M.A.A. Fayed, R.H. Refaey, Y.M. Nissan, Pharmacophore based virtual screening for natural product database revealed possible inhibitors for SARS-COV-2 main protease, Virology 570 (2022) 18–28.
[56] H.A.L. Filipe, L.M.S. Loura, Molecular dynamics simulations: advances and applications, Molecules 27 (2022) 2105.
[57] S. Hossain, A. Parrow, A. Kabedev, R.C. Kneiszl, Y. Leng, P. Larsson, Explicit-pH coarse-grained molecular dynamics simulations enable insights into restructuring of intestinal colloidal aggregates with permeation enhancers, Processes 10 (2022) 29.
[58] M.J. Frisch, G.W. Trucks, H.B. Schlegel, G.E. Scuseria, M.A. Robb, J.R. Cheeseman, J.A. Montgomery Jr., T.K.K.N. Vreven, K.N. Kudin, J.C. Burant, et al., Gaussian 09, Revision D.01, Gaussian, Inc., Wallingford, CT, USA, 2013.
[59] J. Wang, Q. Liu, D. Yang, Theoretical insights into excited-state hydrogen bonding effects and intramolecular proton transfer (ESIPT) mechanism for BTS system, Sci. Rep. 10 (2010) 1–9.

[60] K.A. Peterson, C. Puzzarini, Systematically convergent basis sets for transition metals. II. Pseudopotential-based correlation consistent basis sets for the group 11 (Cu, Ag, Au) and 12 (Zn, Cd, Hg) elements, Theor. Chem. Acc. 114 (2005) 283–296.
[61] B.J. Coe, J.A. Harris, I. Asselberghs, K. Clays, G. Olbrechts, A. Persoons, J.T. Hupp, R.C. Johnson, S.J. Coles, M.B. Hursthouse, K. Nakatani, Quadratic nonlinear optical properties of N-Aryl stilbazolium dyes, Adv. Funct. Mater. 12 (2002) 110–116.
[62] G. Magdy, F. Belal, A.F. Abdel Hakiem, A.M. Abdel-Megied, Salmon sperm DNA binding study to cabozantinib, a tyrosine kinase inhibitor: multi-spectroscopic and molecular docking approaches, Int. J. Biol. Macromol. 182 (2021) 1852–1862.